



Ibrutinib conjugated surface-functionalized multiwalled carbon nanotubes and its biopolymer composites for targeting prostate carcinoma

Raja Murugesan¹, Yuvaraj Haldorai², Linto Sibi³, and Raman Sureshkumar^{1,*} 

¹ Department of Pharmaceutics, JSS College of Pharmacy, JSS Academy of Higher Education, Ooty, Nilgiris, Tamilnadu 643001, India

² Department of Nanoscience and Technology, Bharathiar University, Coimbatore, Tamilnadu 641046, India

³ Department of Physics, PSG College of Arts and Science, Coimbatore, Tamilnadu 641014, India

Received: 4 June 2021

Accepted: 23 September 2021

Published online:

29 September 2021

© The Author(s), under exclusive licence to Springer Science+Business Media, LLC, part of Springer Nature 2021

ABSTRACT

In this report, nanocomposites are composed of surface-functionalized multi-walled carbon nanotubes (f-MWCNTs) and polymers (polyethylene glycol, chitosan) or silver nanoparticles (AgNPs) were successfully synthesized and used as nanocarriers for drug delivery. The drug (Ibrutinib, Ibr) encapsulated with different nanocomposites was used for effective prostate cancer treatment. The as-prepared bioconjugates were confirmed by Fourier transform infrared spectroscopy, X-ray diffraction, and Raman spectroscopy. The drug loading efficiency of 95.5% was achieved for f-MWCNTs/AgNPs composite. The drug release profile showed that the f-MWCNTs/AgNPs composite released 79% in 84 h at pH 5.5 indicating the sustainable drug release. Further, these Ibr-loaded nanocomposites were conjugated with T₃₀ oligonucleotides (T₃₀ ODN) for targeting over-expressed prostate-specific membrane antigen in the prostate gland. The prostate anti-cancer activity was evaluated using PC-3 and MDA-MB-231 cancer cells and the results indicated that the Ibr- loaded nanocomposites conjugated with T₃₀ ODN exhibited higher cell killing efficiency compared to the free Ibr. Therefore, these conjugated nanocomposites are effective drug delivery systems for prostate cancer disease targeted therapy.

Handling Editor: Christopher Blanford.

Address correspondence to E-mail: sureshcoonoor@jssuni.edu.in

Introduction

Prostate cancer (PCa) is one of the most leading cancer observed in men diagnosed in western countries like the USA and Europe [1–3]. According to the Globocon survey-2018, the rate of affected people increased to nearly 4 million wherein the mortality rate rose to 3.82%. The mortality and prevalence level of PCa increased due to lifestyle changes, environmental factors, and genetic factors. Therefore, PCa has become one of the many life-threatening diseases compared to other cancer diseases [4, 5]. The pathophysiology of PCa is the over-expression of prostate-specific membrane antigen (PSMA) in the prostate gland. The PSMA belongs to the family of the glycosylphosphatidylinositol secured cell surface antigens, which have a high level of prostate specificity [6]. Moreover, the major drawback is the detection of PCa. Thus, the level of PSMA has been used as an indicator for screening the PCa [7, 8].

A broad assortment of various nanoscale drug delivery vectors has been evaluated for the treatment of PCa [9–11]. With the advancements in nanotechnology, it has become possible to expand the multifunctional nanostructures like carbon nanotubes (CNTs) involved in the simultaneous detection and treatment of cancer diseases by molecular imaging and therapy technology. Multi-walled carbon nanotubes (MWCNTs) have mainly arisen to be a promising candidate for the competent delivery of drugs and biomolecules due to their structures and physicochemical properties [12, 13]. Unique characteristics of MWCNTs such as size, ultra-lightweight, high surface area, surface chemistry, neutral electrostatic potential, and high drug loading capability make them excellent vehicles for drug delivery, notably on targeting sites [14–20]. In addition to this, they offer probable advantages over the more extensively studied metal complex systems such as efficient drug loading capability, stability, structural flexibility, prolonged circulation time, and bioavailability of carried drug molecules [21, 22]. The MWCNTs based nanocomposites have already been investigated as potential delivery vehicles for intracellular nucleic acids, drug molecules, and proteins. [23–30].

The MWCNTs can be conjugated with the anticancer drug molecules, either by covalent or non-covalent interactions [31]. Also, low molecular weight

targeting agents provided high efficiency for nanotubes' internalization into the cells. However, the first generation of MWCNTs has proven to be inappropriate for drug delivery systems as they bear to agglomerate owing to the poor dispersion in the aqueous medium that makes them incompatible for various pharmacological studies like *in-vitro* and *in-vivo* studies. Consequently, to overcome the aforementioned limitations, the modifications of MWCNTs could be a viable strategy for a therapeutic approach to increase bioavailability. It is reported that the functionalization of MWCNTs with carboxylic functional groups results in enhanced adsorption of the drug molecule due to the intermolecular hydrogen bonding formed between them [32]. Sina et al. [33] simulated the effect of alcohol on the efficiency of doxorubicin (DOX) drug delivery using single-walled carbon nanotubes (SWCNTs). They also investigated the mechanical properties of SWCNTs on DOX adsorption by using molecular dynamic study [34]. Zare et al. [35] summarized promising studies on work regarding the numerous biomedical applications of CNTs as a review. Deb-nath et al. [36] reported the progress and prospects of drug delivery with carbon-based nanomaterials as versatile nanocarriers. Jampilek et al. [37] summarized the latest designed drug delivery nanosystems based on graphene, graphene quantum dots, graphene oxide, reduced graphene oxide, and carbon nanotubes, mainly for anticancer therapy. In addition, MWCNTs coated with synthetic polymers like poly (phenylacetylene), polyethylene glycol (PEG) [38–40], and natural polysaccharide polymers like chitosan (CHI) [41–46] could help in targeted drug delivery. Although excellent progress has been achieved using MWCNTs as drug delivery vehicles, more research is required to promote their capability to accrue in diseased tissues selectively and release their toxic effect in a controlled approach.

We successfully synthesized composites of functionalized MWCNTs with different materials such as PEG, CHI, and silver nanoparticles (AgNPs) for drug delivery. The MWCNTs were prepared by a chemical vapor deposition (CVD) technique, which offers exciting benefits together with large-scale production, low cost, and eco-friendly followed by surface-functionalized with acid groups. The f-MWCNTs-based nanocomposites loaded with Bruton tyrosine kinase inhibitor like Ibrutinib (Ibr) drug conjugated with T₃₀ oligonucleotide (T₃₀ ODN) were used as nanocarriers

to suppress the PSMA so that it can quickly target circulating tumor DNA molecules. Subsequently, the drug incorporation could effectively be administered to the prostate target site. Also, the targeting androgen receptor could help in delivering the drug and suppress the PSMA (Fig. 1). The cytotoxicity studies against PC-3 and MDA-MB-231 cells showed that these composites kill the cells in the targeting site with minimum side effects.

Materials and methods

Materials

Ferrocene, xylene, sulphuric acid, nitric acid, sodium hydrogen phosphate, potassium phosphate, chitosan (CHI), polyethylene glycol (PEG), oleic acid, silver nitrate (AgNO_3 , 99.5%), N, N dimethylformamide (DMF, 98%), and sodium dodecyl sulfate (SDS, 98%) were procured from Sigma Aldrich and SD Fine Chemicals Limited, India. The T_{30} oligonucleotides (T_{30} ODN) were purchased from Bioserve Limited, Hyderabad, India. The chemicals and solvents used

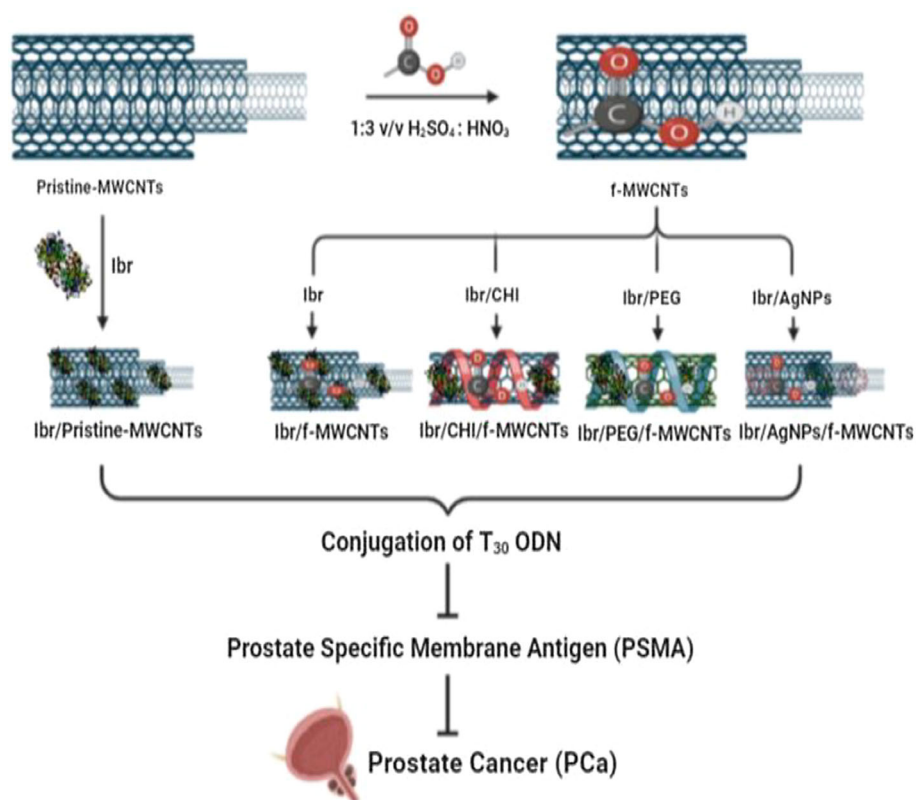
were of analytical grade and were used as such without any further purification.

Methods

Synthesis of MWCNTs

A one-step pyrolysis method was employed for the preparation of MWCNTs using CVD as reported [47]. The schematic diagram is shown in Fig. S1a. The instrumentation portrays the quartz tube reactor (80 cm [L] \times 45 cm [ID]) used for the synthesis in which the temperature profiles were monitored using an adjustable thermocouple. Before initiating the reaction, argon gas (2.5 ml min^{-1}) was passed through the quartz tube for about 10 min to create an oxygen-free ambiance. The ferrocene and xylene precursors were placed in front of the quartz tube reactor where the vaporization of the mixtures gets initiated. The inert carrier gas was employed to transport the carbon and catalyst mixtures to the high-temperature zone ranging from 700 to 1000 $^{\circ}\text{C}$. The heating was switched off after an hour and the system was diminished to room temperature under controlled argon flow. The black deposits of

Figure 1 The schematic diagram of Ibr-loaded MWCNTs-based nanocomposites with T_{30} ODN.



MWCNTs were uniformly deposited at the core region of the reactor and were collected and subjected to further purification process. Amorphous carbon impurities were screened off by heating the collected material at 450 °C for 2 h, whereas the catalyst metal trace was removed using acid treatment. Finally, the product was further washed with an extensive amount of distilled water until pH 7 is attained and dried.

Functionalization of MWCNTs

The functionalized MWCNTs were carried out by the acid reflux method. First, 200 mg of pristine MWCNTs (diameter ~ 50–80 nm) were treated with 100 ml of an acid mixture containing H₂SO₄ and HNO₃ at 1:3 v/v ratio which was then refluxed at 80 °C for 10 h to produce -COOH functionalized MWCNTs (f-MWCNTs). The product was filtered, collected, and washed with double distilled water until the pH turns to neutral. Finally, it was dried under vacuum at 120 °C for 5 h.

Preparation of f-MWCNTs/CHI nanocomposite

The f-MWCNTs (30 mg) were dispersed in CHI solution (60 mg in 60 ml) under sonication for 30 min and stirred at room temperature for 16 h. The f-MWCNTs/CHI nanocomposite was collected and washed with double distilled water by repeated ultracentrifugation until the unbound CHI was removed. It was then dried at room temperature.

Preparation of f-MWCNTs/PEG nanocomposite

Initially, 30 mg of f-MWCNTs were well dispersed in PEG solution (60 mg in 60 ml) using a bath sonicator for 30 min and stirred at room temperature for 16 h. The f-MWCNTs/PEG composite was collected and washed with double distilled water by repeated ultracentrifugation until the unbound PEG was removed. Finally, the f-MWCNTs/PEG nanocomposite was dried at room temperature.

Preparation of f-MWCNTs/Ag nanocomposite

A chemical reduction method was exploited for the synthesis of AgNPs during which a stabilizer and a reducing agent were preferred. At first, 100 mg of f-MWCNTs were well dispersed in DMF containing

0.1 wt% of SDS under continuous stirring wherein the pH was adjusted to neutral. To this, 30 ml of AgNO₃ was added drop by drop under continuous stirring at 40–45 °C followed by sonication for 15 min. The system was kept undisturbed after which the precipitate was collected, washed with distilled water multiple times, and subjected to drying at room temperature to obtain f-MWCNTs/Ag nanocomposite.

Encapsulation of Ibr drug onto the nanocomposite materials

The Ibr (15 mg) drug was mixed with different nanocomposite materials (5 mg) and dispersed in 10 ml of phosphate buffer saline (PBS, pH 7.4), and stirred for 16 h at room temperature. The products were denoted as Ibr/pristine MWCNTs (F1), Ibr/f-MWCNTs (F2), Ibr/f-MWCNTs/CHI (F3), Ibr/f-MWCNTs/PEG (F4), and Ibr/f-MWCNTs/AgNPs (F5). The collected products were washed with PBS by repeated centrifugation to remove the unbound Ibr. The amount of unbound Ibr was determined by the absorbance at 260 nm.

Ibr drug release from the nanocomposite materials

A PBS solution (3.0 ml, pH 5.5, 6.3, and 7.4) containing Ibr-loaded nanocomposite materials (5 mg) were sealed in a dialysis bag (dialysis membrane-150). The dialysis bag was incubated with PBS (7.0 ml) and was allowed to stand at 37 °C under affable shaking for 120 rpm min⁻¹. The amount of Ibr released was measured at different time intervals (0, 12, 24, 36, 48, 60, 72, and 84 h) by using UV–Vis spectrophotometer at 260 nm. All the experiments were repeated thrice.

Conjugation of T₃₀ ODN to Ibr-loaded nanocomposite materials

The Ibr encapsulated nanocomposite materials (10 mg) were suspended in T₃₀ ODN (3 ml) and then sonicated for 30–120 min. The resulting mixtures were incubated for 12 h at 4 °C. After the reaction, combinations of samples were ultracentrifuged for 90 min (1600 rpm) in cold temperature. The product was collected and washed repeatedly with PBS and kept at 4 °C. The conjugation of T₃₀ ODN to Ibr-loaded nanocomposite materials was shown in Fig. S1b.

In-vitro toxicity study

Cell culture

The PC-3 and MDA-MB-231 cells were obtained from the national center for cell science (NCCS), Pune, India. The cells were cultured in Dulbecco's modified eagle medium (DMEM) and minimum essential medium (MEM) at 37 ± 1 °C under a 5% carbon dioxide (CO₂) atmosphere. Each cell culture medium was enhanced with 10% fetal bovine serum (FBS) and washed with a sterilized PBS.

Cytotoxicity assay

The *in-vitro* cytotoxicity test method was performed by MTT (3-(4,5-dimethylthiazole-2-yl)-2,5-diphenyltetra-sodium bromide) cell proliferation assay on PC-3 and MDA MB-231 cell lines for Ibr-loaded nanocomposite materials conjugated with T₃₀ ODN. The cells were trypsinized and counted on a cell hemocytometer. Approximately 10,000 cells per well were seeded in 96-well plates and incubated for 24 h. The culture medium from the PC-3 and MDA MB-231 cells was replaced with a fresh medium. A test sample of different concentrations (5, 50, 100, 150, and 200 µg/ml) were added in triplicates on the cells. After incubation at 37 ± 1 °C for 18 h, the MTT (1 mg/1 ml) was added to all the wells and incubated for 4 h. After incubation, DMSO was added to the wells and read at 570 nm using a photometer. Cell viability and cytotoxicity were calculated by the below formula.

$$\text{Cell viability} = \left(\frac{\text{Treated}}{\text{Control}} \right) \times 100 \quad (1)$$

$$\text{Cytotoxicity} = \left[\frac{(\text{Control} - \text{Treated})}{\text{Control}} \right] \times 100 \quad (2)$$

Apoptosis assay

The apoptosis test was performed by tunnel assay on PC-3 and MDA MB-231 cancer cell lines for Ibr-loaded nanocomposite materials conjugated with T₃₀ ODN. The cells were grown in MEM and DMEM medium supplemented with 10% FBS. The cells ($\sim 10^5$ /well) were seeded in the 24 well plates and incubated in CO₂ at 37 °C for 24 h. The cells after reaching the confluence, test samples were added at different concentrations (5, 50, 100, 150, and 200 µg/

ml) in triplicate. The cells without samples served as a control. The plate was incubated in a CO₂ incubator at 37 °C for 24 h. At the end of incubation, the medium was detached from each well, and cells were washed with PBS (pH 7.4) and established using 80% ethanol. Additionally, acridine orange/ethidium bromide (AO/EtBr) dye (1 mg/ml) was added to each well, incubated for 3–5 min, and imaged the cells using a Nikon camera connected to an inverted phase-contrast fluorescent microscope (Radicals India).

Internalization of the formulation on PC-3 and MDA-MB-231

Based on the release profile of the formulation the internalisation study using the cell lines PC-3 and MDA-MB-231 was carried out. The same has been characterised by using photoluminescence method.

Characterization

Raman spectra were recorded using a Raman spectrometer (Horiba Jobin-LabRam-HR) with an excitation wavelength of 532 nm. An X-ray diffractometer (XRD, Rigagu-Ultima IV) was used for the analysis of the samples from 5 to 80°. Fourier transform infrared spectroscopy (FTIR) was performed using a JASCO 6600 spectrometer. Field emission scanning electron microscopic (FESEM) pictures were obtained using a Hitachi S-4300 microscope. Ultraviolet-visible (UV-vis) spectra were recorded with a Jasco V-650 spectrophotometer. Zeta potential analysis was performed using a Malvern Zetasizer Nano instrument at 25 °C in ultrapure water.

Results and discussion

Characterization of drug-loaded nanocomposite materials

We synthesized different nanocomposites such as f-MWCNTs/CHI, f-MWCNTs/PEG, and f-MWCNTs/Ag and showed good capability as nanocarriers for drug delivery. The drug encapsulated composites were confirmed by UV-visible, XRD, FTIR, and Raman. Figure 2 shows the UV-visible spectra of Ibr-loaded nanocomposite materials. The Ibr loaded systems were luminous in color (ash color) than their

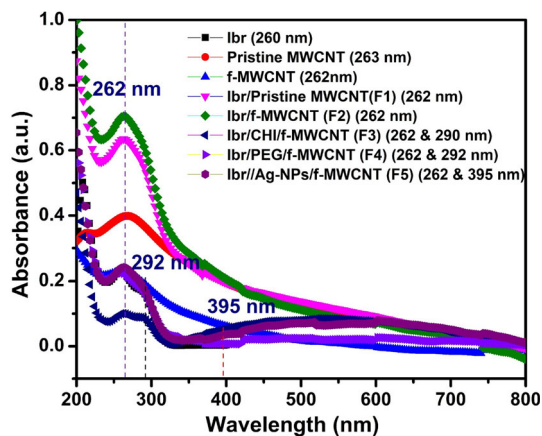


Figure 2 UV–visible absorption spectra of pristine MWCNTs, f-MWCNTs, Ibr/pristine MWCNTs (F1), Ibr/f-MWCNTs (F2), Ibr/f-MWCNTs/CHI (F3), Ibr/f-MWCNTs/PEG (F4), and Ibr/f-MWCNTs/AgNPs (F5).

pioneer. The pure Ibr in water exhibited direct absorption at 260 nm, whereas the peaks of Ibr-loaded nanocomposite materials were marginally red-shifted indicating the interaction between Ibr and MWCNTs with CHI, PEG, and Ag. For comparison, the UV–visible spectra of pristine MWCNTs and f-MWCNTs were also given.

XRD patterns of the MWCNTs and f-MWCNTs-based nanocomposites are shown in Fig. 3a. two peaks were observed at 2θ values of 26.6° and 43.5° in the spectrum of c-MWCNTs, which are attributed to a graphite-like structure which is

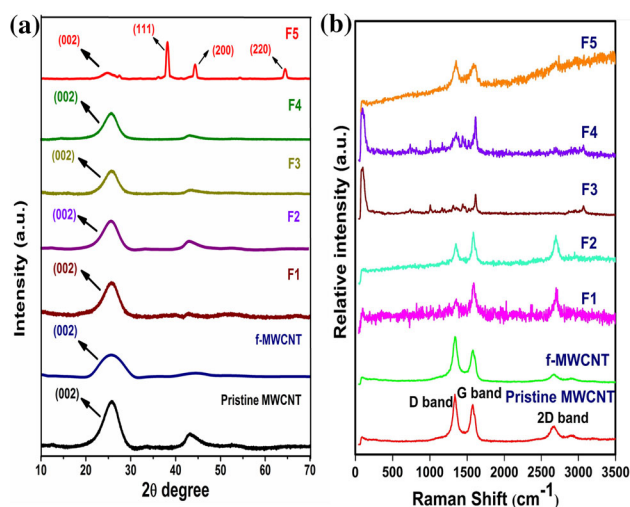


Figure 3 **a** X-ray diffraction and **b** Raman spectra of pristine MWCNTs, f-MWCNTs, Ibr/pristine MWCNTs (F1), Ibr/f-MWCNTs (F2), Ibr/f-MWCNTs/CHI (F3), Ibr/f-MWCNTs/PEG (F4), and Ibr/f-MWCNTs/AgNPs (F5).

attributed to a graphite-like structure [48]. In the case of f-MWCNTs/CHI and f-MWCNTs/PEG nanocomposites, a broad polymer peak was observed at the 2θ value of $20\text{--}25^\circ$ indicating the amorphous nature of the polymers. A small diffraction peak of MWCNTs was observed in the nanocomposite, which may be due to the low amount and relatively low diffraction intensity of MWCNTs. In addition the MWCNTs peak position was overlapped with the polymer peak. In the XRD spectrum of f-MWCNTs/Ag nanocomposite, all the peaks were assigned to Ag and f-MWCNTs. With the exception of the diffraction peak of f-MWCNTs, the peaks at 32.4° , 38.2° , 44.5° , and 64.6° were indexed to the (122), (111), (200), and (220) crystallographic planes of face-centered cubic (fcc) Ag NPs, respectively (JCPDS No. 04–0783) [49]. In additionally, we observed the strong and weak reflections. The that the strong reflections at 2θ of 5.67° , 12.36° , 21.61° , 26.59° corresponds to (002), (200), (222) and (400) planes of MWCNTs (JCPDS No #820,505). The broad peak at 26.59° indicates the presence of graphitic carbon originated from MWCNTs.

The weak reflection at $2\theta = 16.20^\circ$ can be attributed to Ag's (100) plane (JCPDS No#893,081). The examination of $2\theta = 19.03^\circ$ and 10.66° corresponds to PEG and CHI, respectively. It can be deduced from the patterns that no other different peaks are observed, which implicit the purity of the as-prepared formulations. The decrease in the (222) plane's peak intensity depicts effective loading of Ibr into the formulations. It is observed from the results that the peak intensity of the (400) plane decreases with the addition of CHI, PEG and AgNPs with portrays the successful incorporation of CHI, PEG and AgNPs on MWCNTs.

The lattice dynamics and vibration characteristics of carbon-based materials were characterized by employing Raman spectroscopy. Figure 3b reflects the Raman spectra of pristine MWCNTs, f-MWCNTs, and Ibr-loaded nanocomposite materials. The two significant centered at 1339 and 1568 cm^{-1} attributed to D and G bands which arise due to the lattice defects in the MWCNTs and in-plane vibrations of sp^2 carbon atoms. The degree of structural disorder in carbon materials could also be assessed from the D and G band's intensity ratio, where a higher ratio indicates a more significant number of defects [50]. The I_D/I_G ratio for the pristine MWCNTs, f-MWCNTs, Ibr/pristine MWCNTs, Ibr/f-MWCNTs,

Ibr/f-MWCNTs/CHI, Ibr/f-MWCNTs/PEG, and Ibr/f-MWCNTs/AgNPs were calculated as 1.080, 1.110, 0.995, 0.980, 0.988, 0.955 and 1.024, respectively. The drug loading efficiency was enhanced by increasing the structural disorder such as edges, the microstructural arrangement of carbon atoms vacancy, etc. In addition, the f-MWCNTs exhibited higher active sites for efficient loading of CHI, PEG, and AgNPs [51]. Moreover, The I_D/I_G ratio decreases with the addition of CHI, PEG, and AgNPs, which implies the successful incorporation of polymers and metal nanoparticles on the defective site of f-MWCNTs.

The surface morphologies of MWCNTs, f-MWCNTs, and f-MWCNTs-based nanocomposites were examined using FESEM. The pristine MWCNTs morphology was displayed in Fig. 4a as endless, tangled, hollow ropes with smooth surface and the average diameter of each nanotube is less than 30 nm. Figure 4b shows the disentanglement of the f-MWCNTs and slight reduction in the length of the nanotubes is observed after oxidation with acid mixture. Figure 4c and d display the surface adsorption of drug onto the MWCNTs via π - π stacking interaction. In Fig. 4e, the CHI was tightly coated onto the surface of each nanotube and many neighboring MWCNTs were joined together with the CHI at a variety of angles. Similarly, the PEG was also coated on the MWCNTs surface and presented in Fig. 4e. The FESEM image of f-MWCNTs/Ag nanocomposite (Fig. 4g) showed that the AgNPs had a mean diameter of < 20 nm, and were well dispersed in the MWCNTs matrix; however, some nanoparticle aggregation was evident occasionally. The chemical composition of the Ibr/f-MWCNTs/Ag nanocomposite was examined by EDS (Fig. S2). These results confirmed the presence of C, O, and Ag in the nanocomposite. The atomic % of the elements is given as the inset.

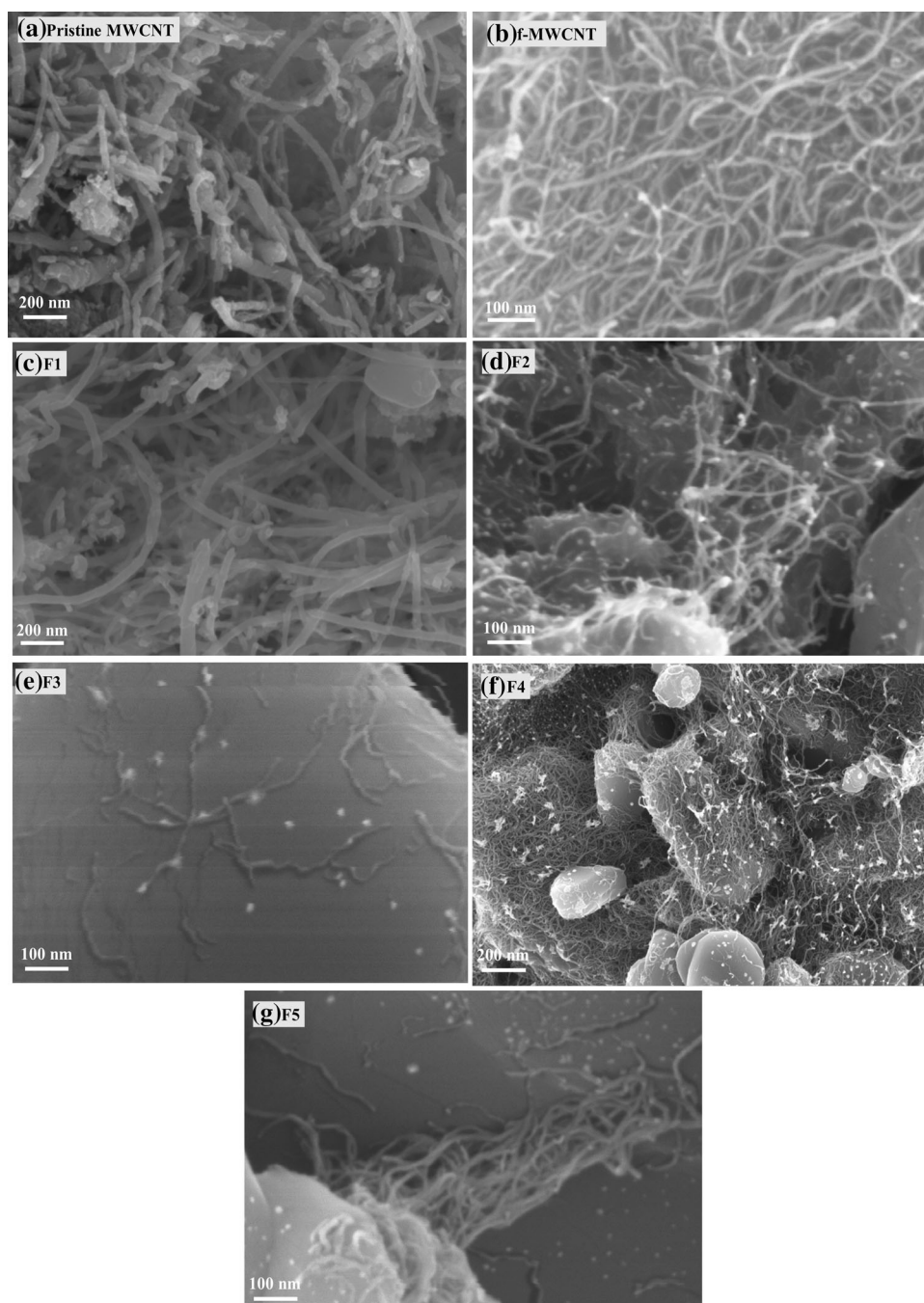
FT-IR spectroscopy is one of the versatile characterization techniques obtained by the interaction of IR radiation with matter, which is used to identify the functional groups present in the material. The FT-IR spectra of MWCNTs, f-MWCNTs, Ibr/pristine MWCNTs, Ibr/f-MWCNTs, Ibr/f-MWCNTs/CHI, Ibr/f-MWCNTs/PEG, and Ibr/f-MWCNTs/AgNPs are shown in Fig. 5. For the pristine MWCNTs, the bands at around 3450 and 1162 cm^{-1} are attributed to the presence of hydroxyl groups ($-\text{OH}$) on the surface of MWCNTs, which could appear either from

ambient moisture bound to the MWCNTs or during the purification of raw material [52]. For the acid-functionalized MWCNTs, the peak near 1560 cm^{-1} corresponds to the IR active phonon mode of the MWCNTs. The presence of carboxylic acid groups on MWCNTs was confirmed with a $\text{C}=\text{O}$ band stretching that appears at around 1741 cm^{-1} . These observations clearly indicate the existence of $-\text{COOH}$ groups on the surface of MWCNTs. In the case of Ibr/f-MWCNTs/CHI nanocomposite, the IR spectrum showed both the peaks of f-MWCNTs and CHI. The band at 3300 cm^{-1} was due to the stretching vibrations of $-\text{OH}$ and $-\text{NH}$ groups of CHI. The peak at 2855 cm^{-1} was attributed to the asymmetric stretching of $-\text{CH}$ group in the polymer, 1648 cm^{-1} indicated the amide I group ($\text{C}-\text{O}$ stretching along the $\text{N}-\text{H}$ deformation), 1584 cm^{-1} was due to $-\text{NH}$ deformation, 1345 cm^{-1} was attributed to the COO -group in carboxylic acid salt and 1045 cm^{-1} was assigned to the stretching vibration of $\text{C}-\text{O}-\text{C}$ in glucose circle [53]. From the FTIR spectrum of f-MWCNTs/PEG nanocomposite, $\text{C}=\text{C}$ stretching mode of the aromatic ring was observed between 1636 cm^{-1} and 1540 cm^{-1} . The stretching vibration of $>\text{C}=\text{O}$ in ester at 1718 cm^{-1} , asymmetric and symmetric stretching of $\text{C}-\text{H}$ deformation at 2983 and 2878 cm^{-1} were also found in the spectrum, which were not found in the spectrum of the other samples. It could also be observed that the stretching vibrations of the repeating $-\text{OCH}_2\text{CH}_2$ units of PEG and $-\text{COO}$ bonds were at 1099 cm^{-1} and 1239 cm^{-1} respectively, which is proof of a successful formation of composite. In the case of f-MWCNTs/Ag nanocomposite, we observed only the f-MWCNTs peaks[54]. For reference, the FT-IR spectra of pure Ibr, CHI, PEG, and AgNO_3 were given in Fig. S3.

Ibr-loading onto the MWCNTs-based nanocomposites

The drug loading activities are one of the most notable characteristics to evaluate DDS. The pristine and f-MWCNTs can easily adsorb the drug molecule in the sidewalls of the MWCNTs owing to the π - π interaction. The drug loading into the pristine MWCNTs, f-MWCNTs, f-MWCNTs/CHI, f-MWCNTs/PEG, and f-MWCNTs/AgNPs was determined by UV – visible spectroscopy. The loading was achieved by stirring the drug with the nanomaterials (f-MWCNTs CHI or PEG or AgNPs) in PBS, followed by centrifugation, washing

Figure 4 FESEM images of **a** pristine MWCNTs, **b** f-MWCNTs, **c** lbr/pristine MWCNTs (F1), **d** lbr/f-MWCNTs (F2), **e** lbr/f-MWCNTs/CHI (F3), **f** lbr/f-MWCNTs/PEG (F4), and **g** lbr/f-MWCNTs/AgNPs (F5).



with PBS, and freeze-drying. The amount of drug and the nanomaterials were 15 mg and 5 mg, respectively. The amount of drug-loaded into the nanomaterial is shown in Fig. 6a. The drug loading efficiency onto the nanomaterials was in the given order of pristine MWCNTs > f-MWCNTs > f-MWCNTs/CHI > f-MWCNTs/PEG > f-MWCNTs/AgNPs. The maximum drug loading efficiency of 95.5% was observed for

f-MWCNTs/Ag nanocomposite. Zeta potential, that is, surface charge, can greatly influence particle stability in suspension through electrostatic repulsion between particles. It mainly aids in the nanoparticle interaction with any species which is usually negatively charged. Table 1 shows the zeta potential values of different nanomaterials.

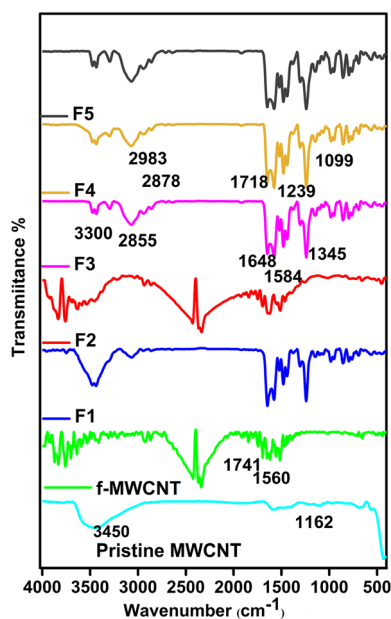


Figure 5 FT-IR spectra of pristine MWCNTs, f-MWCNTs, Ibr/pristine MWCNTs (F1), Ibr/f-MWCNTs (F2), Ibr/f-MWCNTs/CHI (F3), Ibr/f-MWCNTs/PEG (F4), and Ibr/f-MWCNTs/AgNPs (F5).

Ibr release from MWCNTs-based nanocomposites

The drug release profiles of Ibr-loaded MWCNTs-based nanocomposites at 37 °C in PBS at different pH

Figure 6 **a** Drug loading profile and **b–d** drug release profiles at different pH values (7.4, 6.3, and 5.5). The error bar represents the SD (standard deviation) of three independent experiments.

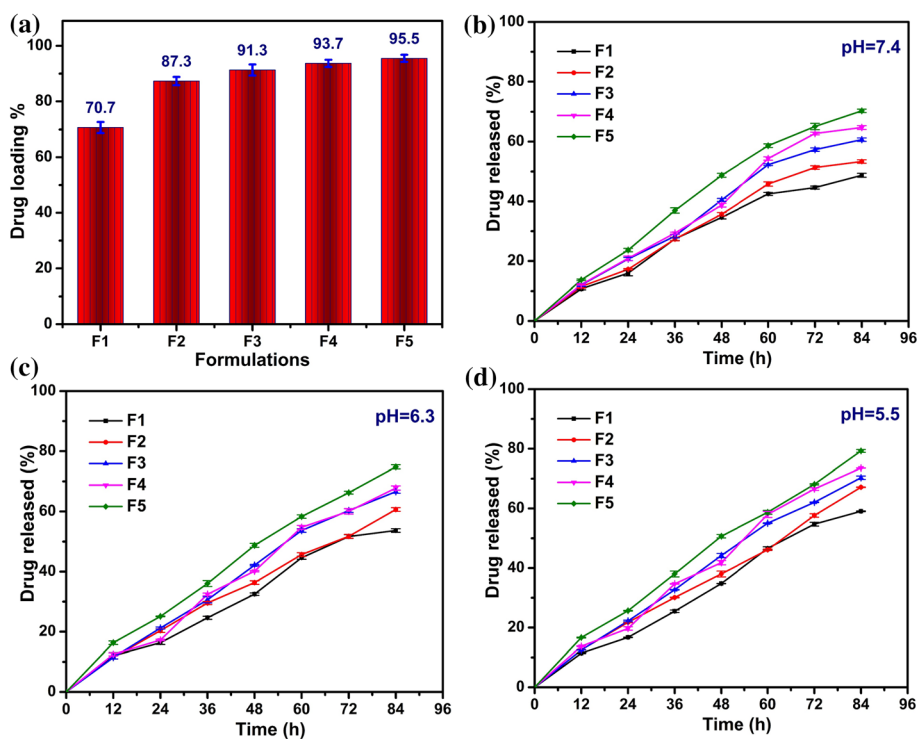


Table 1 Zeta potential values of MWCNTs-base nanocomposites

S. No	Nanomaterials	Zeta potential (mV)
1	MWCNTs	− 22.7
2	f-MWCNTs	− 19.1
3	f-MWCNTs/CHI	− 5.2
4	f-MWCNTs/PEG	− 2.2
5	f-MWCNTs/AgNPs	− 2

values (7.4, 6.3, and 5.5) are shown in Fig. 6b–d. The pH of 7.4, 6.3, and 5.5 corresponds to the physiological and lysosomal pH of the cancer cells, and a noticeable release of Ibr from all the MWCNTs-based nanocomposites was observed for 84 h. The drug release patterns of nanocomposites was slow at pH 7.4 ($48 \pm 0.6\%$, $53 \pm 0.6\%$, $61 \pm 0.6\%$, $65 \pm 0.6\%$, and $70 \pm 0.6\%$) and pH 6.3 ($54 \pm 0.6\%$, $61 \pm 0.6\%$, $67 \pm 0.5\%$, $68 \pm 0.7\%$, and $75 \pm 0.7\%$) compared to pH 5.5. The drug release rate was higher at pH 5.5 due to the weakening of the hydrogen bond between Ibr and MWCNTs. The amount of drug released was $59 \pm 0.1\%$, $67 \pm 0.1\%$, $70 \pm 0.6\%$, $74 \pm 0.1\%$, and $79 \pm 0.5\%$ at different time intervals such as 12, 24, 36, 48, 60, 72, and 84 h, respectively. The drug release experiments were done in triplicate and the mean standard deviation values were calculated.

In-vitro cytotoxicity studies of Ibr-loaded MWCNTs-based nanocomposites conjugated with T₃₀ ODN

The sequences of *in-vitro* studies have been conducted to determine the cytotoxicity profile of Ibr/pristine MWCNTs, Ibr/f-MWCNTs, Ibr/f-MWCNTs/CHI, Ibr/f-MWCNTs/PEG, and Ibr/f-MWCNTs/AgNPs nanocomposites conjugated with T₃₀ ODN using the conventional MTT cell proliferation assay (Fig. 7). The effects of these nanocomposites were evaluated against two cell lines namely PC-3 (Fig. 7a) and MDA-MB-231 (Fig. 7b), which are known to be prostate and breast cancer cells. All the nanocomposites showed lower cell viability against both the cell lines compared to the pure Ibr in all the concentration ranges (5 to 200 $\mu\text{g ml}^{-1}$). Moreover, the lower cell viability (< 30%) of Ibr/f-MWCNTs/Ag nanocomposite indicates that the cytotoxicity of the nanocomposite was negligible. The optical images are shown in Fig. S4 indicate that the Ibr rapidly accumulates inside the cancer cells and targets the particular site. These data suggest that the Ibr has been released sustainably. The higher killing ability of Ibr-loaded MWCNTs nanocomposites against the PC-3 and MDA-MB-231 indicates that these composites delivered more Ibr which suppresses the over-expressed PSMA [55–57].

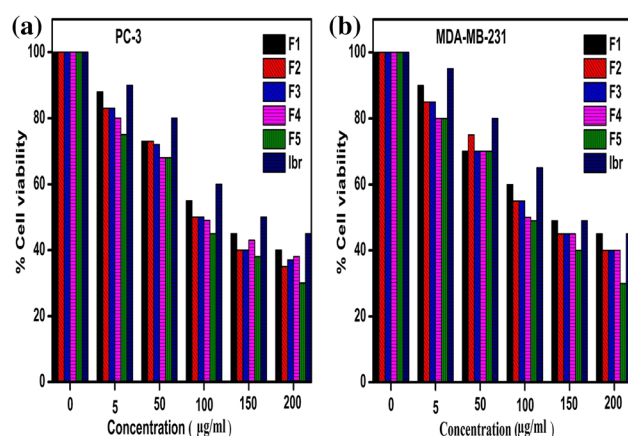


Figure 7 Cell viability of Ibr/pristine MWCNTs (F1), Ibr/f-MWCNTs (F2), Ibr/f-MWCNTs/CHI (F3), Ibr/f-MWCNTs/PEG (F4), Ibr/f-MWCNTs/AgNPs (F5), and pure Ibr samples after treated with **a** PC-3 cell line and **b** MDA-MB-231 cell line for 24 h.

Apoptosis assay of Ibr-loaded MWCNTs-based nanocomposites conjugated with T₃₀ ODN

Apoptosis assay was evaluated to determine the apoptotic level of Ibr/pristine MWCNTs, Ibr/f-MWCNTs, Ibr/f-MWCNTs/CHI, Ibr/f-MWCNTs/PEG, and Ibr/f-MWCNTs/AgNPs nanocomposites conjugated with T₃₀ ODN by fluorescent tunnel labeling method. Two different cell lines such as PC-3 and MDA-MB-231 were evaluated. Fig. S5 shows the positive apoptotic cells for both cell lines. These are fragmented nuclei due to the fluorescent-labeled and the viable cells not being labeled. The maximum concentration of $\sim 200 \mu\text{g mL}^{-1}$ of nanocomposites showed excellent activity at 74 h against both the cell lines [58, 59].

Internalization of the formulation on PC-3 and MDA-MB-231

The Ibr showed good photoluminescent property with maximum excitation and emission wavelength at 280 nm and 420 nm for both free Ibr and drug-loaded and it is shown in the below Fig. 8.

As per the release studies mentioned in the Sect. [Ibr release from MWCNTs-based nanocomposites](#) it is apparent that the prepared F5 formulations viz., MWCNT formulated composites like MWCNT/Ag composite shows high drug release at the lysosomal pH (pH-5.5) when compared to other prepared composites. Hence we used this formulation to evaluate the drug internalization. The internalisation was confirmed with photoluminescence method. From the study, it is also clear that the drug itself exhibits some fluorescence and the same has been compared with the F5 formulation.

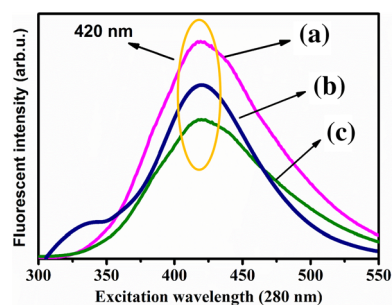


Figure 8 Photoluminescent spectra of **a** Free Ibr, **b** drug-loaded F5 nanocomposite on PC-3 and **c** MDA-MB 231 at the excitation wavelength of 280 nm.

Then Ibr loaded MWCNT/Ag nanocomposite (200 µg/mL) was treated with PC-3 and MDA-MB 231 cells for 12 h. Then the cells were washed 3 times with PBS buffer and harvested via trypsinization. The cells were again washed for 3 times with PBS buffer then analyzed with photoluminescent spectroscopy at the excitation wavelength of 280 nm with an emission peak at 420 nm. The result showed that the F5 drug-loaded nanocomposite treated PC-3 and MDA-MB 231 cells showed significant peak intensity of Ibr at 420 nm. This confirms the successful internalization of drug inside the cell.

Conclusion

Herein, a highly effective DDS based on the f-MWCNTs and their composites with CHI, PEG, and AgNPs were prepared and used as nanocarriers. Among the nanocomposite, the f-MWCNTs/Ag nanocomposite exhibited higher drug encapsulation efficiency of 95.5%. The drug release profiles showed that the f-MWCNTs/Ag nanocomposite released 70%, 75%, and 79% of the drug at different pH values of 7.4, 6.3, and 5.5, respectively in 84 h. The higher release of drug at pH 5.5 may be attributed to the fact that the surface negative charges decrease which facilitates the fast release of drug from the nanocarrier. Besides, the Ibr- loaded nanocomposites easily conjugated with the T₃₀ ODN and enhanced the apoptotic cell in over-expression of PSMA. Moreover, the nanocomposites showed excellent cytotoxicity on the MDA-MB-231 and PC-3 cancer cell lines. In this strategy, we conclude that the f-MWCNTs/CHI, f-MWCNTs/PEG, and f-MWCNTs/Ag nanocomposites delivered the drug more effectively than the pristine MWCNTs and f-MWCNTs. These actual merits attribute to make further detection and diagnosis of the *in-vivo* system.

Acknowledgements

This work is financially supported by the JSS Academy Higher Education and Research (JSSAHER), Mysuru. Award No: REG/DIR(R) /JSSURF/29(1)/2020-11. I would like to acknowledge Dr. Yuvaraj Haldorai (DBT Ramalingasamy Fellow (BT/RLF/Re-entry/48/2015), Department of Nanoscience and

Technology, Bharathiar University, Coimbatore, Tamilnadu, India.

Declarations

Conflict of interest The authors declare that they have no conflict of interest.

Supplementary Information: The online version contains supplementary material available at <https://doi.org/10.1007/s10853-021-06559-w>.

References

- [1] Ferlay J (2018) Cancer incidence and mortality patterns in Europe: estimates for 40 countries and 25 major cancers in 2018. *Eur J Cancer* 103:356–387
- [2] Siegel RL, Miller KD, Jemal A (2019) Cancer statistics, CA Cancer. *J Clin* 69:7–34
- [3] Rawla P (2019) Epidemiology of prostate cancer. *World J Oncol* 10:63–89
- [4] Bray F, Ferlay J, Soerjomataram I (2018) Global cancer statistics 2018: GLOBOCAN estimates of incidence and mortality worldwide for 36 cancers in 185 countries *CA Cancer. J Clin* 6:394–424
- [5] Stewart BW, Wild CP (2014) World Cancer Report, International Agency for Research on Cancer, Lyon, France (2014). ISBN: 978–92–832–0429–9.
- [6] Lam JS, Yamashiro J, Shintaku IP, Vessella RL, Jenkins RB, Horvath S (2005) Prostate stem cell antigen is overexpressed in prostate cancer metastases. *Clin Cancer Res* 11:2591–2596
- [7] Dhanasekaran SM, Barrette TR, Ghosh D, Shah R, Varambally S, Kurachi K, Pienta KJ, Rubin MA, Chinnaiyan AM (2001) Delineation of prognostic biomarkers in prostate cancer. *Nature* 412:822–826
- [8] Heidenreich A, Bastian PJ, Bellmunt J, Bolla M, Joniau S, van der Kwast T, Mason M, Matveev V, Wiegel T, Zattoni F, Mottet N (2014) EAU guidelines on prostate cancer. Part 1: screening, diagnosis, and local treatment with curative intent-update 2013. *Eur Urol* 65:124–137
- [9] Pan DJ, Turner JL, Wooley KL (2004) Shell cross-linked nanoparticles designed to target angiogenic blood vessels via alpha(v)beta(3) receptor-ligand interactions. *Macro mole* 37:7109–7115
- [10] Chithrani BD, Ghazani AA, Chan WCW (2006) Determining the size and shape dependence of gold nanoparticle uptake into mammalian cells. *Nano Lett* 6:662–668
- [11] Endo M, Strano MS, Ajayan PM (2008) Potential applications of carbon nanotubes. In: Jorio A, Dresselhaus G,

- Dresselhaus MS (eds) Topics in applied physics. Springer, Berlin
- [12] Bottini M, Rosato N, Bottini N (2011) PEG-modified carbon nanotubes in biomedicine: current status and challenges ahead. *Biomacromolecule* 12:3381–3393
- [13] Prakash S, Malhotra M, Shao W, Tomaro-Duchesneau C, Abbasi S (2011) Polymeric nanohybrids and functionalized carbon nanotubes as drug delivery carriers for cancer therapy. *Adv Drug Deliv Rev* 63:340–351
- [14] Kam NWS, Jessop TC, Wender PA, Dai HJ (2004) Nanotube molecular transporters: internalization of carbon nanotube–protein conjugates into mammalian cells. *J Am Chem Soc* 126:6850–6851
- [15] Kam NWS, O’Connell M, Wisdom JA, Dai HJ (2005) The properties of transparent ductivity oxides ITO deposited on flexible substrate. *Proc Natl Acad Sci USA* 102:11600
- [16] Kam NWS, Dai HJ (2005) Carbon Nanotubes as Intracellular Protein Transporters: Generality and Biological Functionality. *J Am Chem Soc* 127(16):6021–6026
- [17] Feazell RP, Nakayama-Ratchford N, Dai HJ, Lippard SJ (2007) Soluble single-walled carbon nanotubes as longboat delivery systems for platinum(IV) anticancer drug design. *J Am Chem Soc* 129(27):8438–8439
- [18] Foldvari M, Bagonluri M (2008) Carbon nanotubes as functional excipients for nanomedicines: II Drug delivery and biocompatibility issues. *Nanomedicine* 4(3):183–200
- [19] Liu J, Zubiri MRI, Dossot M, Vigolo B, Hauge RH, Fort Y, Ehrhardt JJ, McRae E (2006) Sidewall functionalization of single-wall carbon nanotubes (SWNTs) through aryl free radical addition. *Chem Phys Lett* 430:93–96
- [20] Zhang XK, Meng LJ, Lu QG, Fei ZF, Dyson PJ (2009) Targeted delivery and controlled release of doxorubicin to cancer cells using modified single-wall carbon nanotubes. *Biomaterials* 30:6041–6047
- [21] Pastorin G, Wu W, Wieckowski S, Briand JP, Kostarelos K, Prato M, Bianco A (2006) Double functionalization of carbon nanotubes for multimodal drug delivery. *Chem Commun.* <https://doi.org/10.1039/B516309A>
- [22] Rafeeqi T, Kaul G (2011) Elucidation of interaction between multi-walled carbon nanotubes and cell culture medium by spectroscopy supports biocompatibility of these nanotubes. *Adv Sci Lett* 4:536–540
- [23] Kam NWS, Liu Z, Dai H (2006) Carbon nanotubes as intracellular transporters for proteins and DNA: an investigation of the uptake mechanism and pathway. *Angew Chem* 118:591–595
- [24] Zhang Z, Yang X, Zhang Y, Zeng B, Wang S, Zhu T, Roden RB, Chen Y, Yang R (2006) Delivery of telomerase reverse transcriptase small interfering RNA in complex with positively charged single-walled carbon nanotubes suppresses tumor growth. *Clinical Cancer Res* 12:4933–4939
- [25] Ali-Boucetta H, Al-Jamal KT, McCarthy D, Prato M, Bianco A, Kostarelos K (2008) Multiwalled carbon nanotube-doxorubicin supramolecular complexes for cancer therapeutics. *Chem Commun.* <https://doi.org/10.1039/B712350G>
- [26] Huang W, Taylor S, Fu K, Lin Y, Zhang D, Hanks TW, Rao AM, Sun YP (2002) Attaching proteins to carbon nanotubes via diimide-activated amidation. *Nano Lett* 2:311–314
- [27] Baker SE, Cai W, Lasserter TL, Weidkamp KP, Hamers RJ (2002) Covalently bonded adducts of deoxyribonucleic acid (DNA) oligonucleotides with single-wall carbon nanotubes: synthesis and hybridization. *Nano Lett* 2:1413–1417
- [28] Yu BZ, Yang JS, Li WX (2007) In vitro capability of multi-walled carbon nanotubes modified with gonadotrophin-releasing hormone on killing cancer cells. *Carbon* 45:921–927
- [29] Yinghui Z, Peng AT, Carpenter K, Maguire JA, Hosmane NS, Takagaki M (2005) Substituted carborane-appended water-soluble single-wall carbon nanotubes: a new approach to boron neutron capture therapy drug delivery. *J Am Chem Soc* 127:9875–9880
- [30] Wu W, Wieckowski S, Pastorin G, Benincasa M, Klumpp C, Briand JP, Gennaro R, Prato M, Bianco A (2005) Targeted delivery of amphotericin B to cells by using functionalized carbon nanotubes. *Angew Chem Int Ed* 44:6358–6362
- [31] Vashist SK, Zheng D, Pastorin G, Al-Rubeaan K, Luong JHT, Sheu FS (2011) Delivery of drugs and biomolecules using carbon nanotubes. *Carbon* 49:4077–4097
- [32] Sina K, Babak S, Tien C (2021) Theoretical investigation of adsorption mechanism of doxorubicin anticancer drug on the pristine and functionalized single walled carbon nanotube surface as a drug delivery vehicle: A DFT study. *J Mol Liquids* 322:114890
- [33] Sina K, Babak S, Tien C (2021) Prediction effect of ethanol molecules on doxorubicin drug delivery using single walled carbon nanotube carrier through POPC cell membrane. *J Mol Liquids* 330:115698
- [34] Sina K, Babak S, Tien C (2020) Investigate the importance of mechanical properties of SWCNT on Doxorubicin anticancer drug adsorption for medical application: a molecular dynamic study. *J Mol Grap Modell* 101:107745
- [35] Zare H, Ahmadi S, Ghasemi A, Ghanbari M, Rabiee N, Bagherzadeh M, Karimi M, Webster TJ, Hamblin MR, Mostafavi E (2021) Carbon nanotubes: smart drug/gene delivery carriers *Int J. Nanomed* 16(1681):1706
- [36] Debnath SK, Srivastava R (2021) Drug delivery with carbon-based nanomaterials as versatile nanocarriers: progress and prospects. *Front Nanotechnol* 3:644564

- [37] Jampilek J, Kralova K (2021) Advances in drug delivery nanosystems using graphene-based materials and carbon nanotubes. *Materials* 14:1059
- [38] Tang BZ, Xu HY (1999) Preparation, alignment, and optical properties of soluble poly(phenylacetylene)-wrapped carbon nanotubes. *Macromolecule* 32:2569–2576
- [39] Yuan WZ, Sun JZ, Dong YQ, Haussler M, Yang F, Xu HP (2006) Wrapping carbon nanotubes in pyrene-containing poly(phenylacetylene) chains: solubility, stability, light emission, and surface photovoltaic properties. *Macromolecule* 39:8011–8020
- [40] Nozomi NR, Sarunya B, Xiaoming S, Kevin W, Hongile D (2007) Noncovalent functionalization of carbon nanotubes by fluorescein- polyethylene glycol: supramolecular conjugates with pH-dependent absorbance and fluorescence. *J Am Chem Soc* 9:2448–2449
- [41] Abarrategi A, Gutierrez MC, Moreno-Vicente C, Hortiguella MJ, Ramos V, Lopez-Lacomba JL (2008) Multiwall carbon nanotube scaffolds for tissue engineering purposes. *Biomaterials* 29:94–102
- [42] Fu C, Meng L, Lu Q, Zhang X, Gao C (2007) Large-scale production of homogeneous helical amylose/SWNTs complexes with good biocompatibility. *Macromol Rapid Commun* 28:2180–2184
- [43] Hasegawa T, Fujisawa T, Numata M, Umeda M, Matsumoto T, Kimura T (2004) Single-walled carbon nanotubes acquire a specific lectin-affinity through supramolecular wrapping with lactose-appended schizophyllan. *Chem Commun* 4(19):2150–2151
- [44] Long DW, Wu GZ, Zhu GL (2008) Non covalently modified carbon nanotubes with carboxymethylated chitosan: a controllable donor-acceptor nanohybrids. *Int J Mol Sci* 9:120–130
- [45] Numata M, Asai M, Kaneko K, Hasegawa T, Fujita N, Kitada Y (2004) Curdlan and schizophyllan (beta-1,3-glucans) can entrap single-wall carbon nanotubes in their helical superstructure. *Chem Lett* 33:232–233
- [46] Zhang XK, Wang XF, Lu QH, Fu CL (2008) Influence of carbon nanotube scaffolds on human cervical carcinoma HeLa cell viability and focal adhesion kinase expression. *Carbon* 46:453–460
- [47] Rajavel K, Dinesh M, Saranya R, Rajendra Kumar RT (2015) Enhanced vacuum sensing performance of multi-walled carbon nanotubes: role of defects and carboxyl functionalization. *RSC Adv* 5:20479–20485
- [48] Yuvaraj H, Jeong YT, Lee WK, Lim KT (2009) Synthesis of MWNT/PEDOT composites for the application of organic light emitting diodes. *Mol Cryst Liq Crystal* 514:366–374
- [49] Anchu A, Anand K, Janarthanan P, Mansour SA (2020) Synthesis and growth mechanism of bamboo-like N-doped CNT/graphene nanostructure incorporated with hybrid metal nanoparticles for overall water splitting. *Carbon* 170:452–463
- [50] Heise HM, Kuckuk R, Ojha AK, Srivastava A, Srivastava V, Asthana BP (2009) Characterisation of carbonaceous materials using Raman spectroscopy: a comparison of carbon nanotube filters, single- and multi-walled nanotubes, graphitized porous carbon and graphite. *J Raman Spectrosc* 40:344–353
- [51] Wei B, Achyut R, Ramakrishna P, Jared MB (2016) Defect density in multiwalled carbon nanotubes influences ovalbumin adsorption & promotes macrophage activation and CD4 T-Cell proliferation. *Int J Nanomed* 11:4357–4371
- [52] Haldorai Y, Si W, Jae-Jin S (2013) Poly(aniline-co-*p*-phenylenediamine)/MWCNT nanocomposites via in situ microemulsion: synthesis and characterization. *Colloid Polym. Sci* 287:1273–1280
- [53] Yuvaraj H, Jae-Jin S (2014) An efficient removal of methyl orange dye from aqueous solution by adsorption onto chitosan/MgO composite: A novel reusable adsorbent. *Appl Surf Sci* 292:447–453
- [54] Sharmeen S, Rahman AM, Lubna MM, Salem KS, Islam R, Khan MA (2018) Polyethylene glycol functionalized carbon nanotubes/gelatin-chitosan nanocomposite: An approach for significant drug release. *Bioact Mater* 3:236–244
- [55] Ling Y, Wei K, Luo Y, Gao X, Zhong SZ (2011) Dual docetaxel/superparamagnetic iron oxide loaded nanoparticles for both targeting magnetic resonance imaging and cancer therapy. *Biomaterials* 32:7139–7150
- [56] Huxia W, Haili S, Hao Z, Xue W, Yan Y (2014) Prostate stem cell antigen-antibody- conjugated multiwalled carbon nanotubes for targeted ultrasound imaging and drug delivery. *Biomaterials* 35:5369–5380
- [57] Zhang Z, Ling L, Qi L, Chong Y, Xue L (2020) Bruton's tyrosine kinase (BTK) inhibitor (Ibrutinib)- suppressed migration & invasion of prostate cancer. *Oncol Ther* 1:4113–4122
- [58] Chan FL, Choi HL, Chen ZY, Chan SF, Huang Y (2000) Induction of apoptosis in prostate cancer cell lines by a flavonoid, baicalin. *Cancer Lett* 160:219–228
- [59] Xiongwen Z, Steiner MS, Rinalds A, Yi L (2001) Apoptosis induction in prostate cancer cells by novel gene product, pHyde, involves caspase-3. *Oncogen* 20:5982–5990

Publisher's Note Springer Nature remains neutral with regard to jurisdictional claims in published maps and institutional affiliations.